*Veena Vijayan Krishnakumari[1], Preetha Soman Nair[1], Sarath Kumar Muraleedharan Nair Sarala Devi[1], Sajan Davidson[2], Jolly Bose Raghavan Pillai[1,3]**

[1]Department of Physics, Government College Kariavattom, Thiruvananathapuram, Kerala, India, [2]Department of Physics, Bishopmoore College, Mavelikkara, Alapuzha, Kerala,India, [3]Principal, BJM Government College Chavara, Kollam, University of Kerala, India.

Scientific paper
ISSN 0351-9465, E-ISSN 2466-2585
https://doi.org/10.62638/ZasMat1830

Zastita Materijala 67 ()
(2026)

A simple strategy for synthesizing copper tungstate nanoparticles with enhanced chemocatalytic degradation

ABSTRACT

The ever-increasing demand for efficient and sustainable catalytic systems has promoted a surge in the exploration of transition metal nanoparticles as catalysts for various chemical reactions. $CuWO_4$ nanoparticles were formed by co-precipitating copper chloride and sodium tungstate in a 1:1 molar ratio. The nanoparticles were characterized extensively by using various techniques including, X-ray diffraction (XRD), Raman Spectroscopy, Fourier transform infrared (FTIR) spectroscopy, Ultraviolet-visible diffuse reflectance spectroscopy (UV-DRS), Brunauer-Emmett-Teller (BET), X-ray photoelectron spectroscopy (XPS), Energy Dispersive Spectroscopy (EDS) and Photoluminescence (PL) measurements. The XRD and RAMAN studies revealed the presence of water molecules in the lattice of the as-synthesized and sample heat treated at 300 °C, indicating that the material is copper tungstate dihydrate ($CuWO_4 \cdot 2H_2O$) with a monoclinic structure. In contrast, the samples heat-treated at 400 °C, 500 °C and 600 °C exhibited an anorthic (triclinic) structure of $CuWO_4$.XRD data was used to calculate the average grain size and lattice parameters. The FT-IR analysis confirms the formation $CuWO_4$ nanoparticles. The Diffuse reflectance ultraviolet-visible spectroscopy, the obtained band gaps of nanoparticles ranging from 2.9 to 2.2 eV, measured using the Kubelka and Munk method. The Brunauer-Emmett-Teller (BET) specific surface area analysis provided insights in to availability of active surface sites in $CuWO_4$ nanostructures. Elemental analysis and chemical composition of $CuWO_4$ were determined using X-ray photoelectron spectroscopy (XPS) and Energy Dispersive Spectroscopy (EDS), which confirms the presence of peaks corresponding to W, O, and Cu only. Photoluminescence (PL) studywith an excitation wavelength of 290 nm reveals that for all the samples the emissions appeared at wavelengths between 400 and 500 nm. The catalytic activity of $CuWO_4$ nanoparticles was assessed by measuring the breakdown of the methylene blue dye. This study reports a novel synthesis of $CuWO_4$ as an efficient chemocatalyst, achieving a catalytic degradation of approximately 98.3%, which can have potential applications in wastewater management.

Keywords: *Copper tungstate, Chemocatalysis, Co-precipitation method, XRD, UV-Vis, BET, XPS.*

1. INTRODUCTION

Water and environmental pollution have escalated alongside changing lifestyles, rapid urbanization, industrialization, and advancements in agricultural practices. Primary sources of contamination include municipal, agricultural, and industrial waste, often resulting in large-scale effluent discharges [1-3]. The textile industry is a major contributor to pollution, frequently releasing untreated effluent into rivers or soil without adhering to proper treatment protocols.

This effluent typically contains electrolytes, surfactants, heavy metals, and dyes, with dyes being the most persistent pollutants due to their chemical stability and resistance to biodegradation. Their presence damages human health as well as underwater habitats [4-9]. The unique properties and extensive applications of nanomaterials arise from their size, surface structure, and interparticle interactions. Nanostructured tungstate materials have garnered attention for their potential applications, luminescent properties, and distinctive structural characteristics. Transition metal tungstates, represented as AWO_4 (where A commonly includes Cu, Mn, Mg, Zn, Cd, Fe, Co, or Ni), are ternary oxide semiconductors recognized for their exceptional photoelectrochemical, electrocatalytic, luminescent, and photocatalytic properties [10,11]. These materials have been

*Corresponding author: Jolly Bose R Principal, BJM Government College Chavara, Kollam, Kerala, India
E-mail: jollyboser@gmail.com
Paper received: 04. 05.2026.
Paper accepted: 06. 06, 2026.

effectively used in a wide range of technological applications, such as solid-state lasers, optical fibers, fluorescent lighting, humidity sensors, and optoelectronic devices. Furthermore, a number of metal tungstates have unique conductivity and electrical properties [12]. Metallic cations with radii smaller than 0.077 nm are more likely to create wolframite-type tungstates, whereas those with radii greater than 0.099 nm are more likely to form scheelite-type tungstates [13]. $[AO_6]/[WO_6]$ the transition metal (A) and tungsten (W) atoms join with six oxygen atoms to form groups in wolframite-type monoclinic structures. The scheelite structures, however, involve the creation of $[AO_8]/[WO_4]$ groups, in which the W atom forms a link with four oxygen atoms and the transition metal (A) forms a binding with eight [14–16]. With an indirect bandgap energy ranging from 2.2 to 2.45 eV [17–19], $CuWO_4$, or copper tungstate, is an n-type semiconductor that is nontoxic, chemically stable, and capable of efficiently utilizing sunlight. WO_6 and CuO_6 octahedra shape and coupling have a major impact on the bandgap [20, 21]. $CuWO_4$'s photoelectrochemical water splitting and photoelectrocatalytic activity are made possible by these properties [22–24].

Research on copper tungstate has garnered significant notice because to its many potential technological [25] and scientific applications including photoanodes [17], scintillation detectors, gas and humidity sensors [26,27], supercapacitors [28–30], electrochromic devices [28,31], photoelectrolysis electrodes for lithium-ion batteries [32–34], and photoelectrodes [35]. Various morphologies of copper tungstate have on created by utilizing a range of physical and chemical techniques, including the electrochemical approach [36], spray pyrolysis [37], solid-state reactions [38], pulsed laser deposition [39], and precipitation routes [40, 41]. For many years, organic pollutants have been mineralized using compounds from the tungstate family under UV [42] and sunlight [43].

Ruiz-Fuertes et al. [21] studied the growth and characterization of $CuWO_4$ under high pressure. Using the microemulsion technique, Maryam Mohammadikish and associates [44] examined the optical characteristics of copper tungstate nanoparticles. Hierarchical flower-like WO_3 nanoparticles were created by Ghedeir M. Alshammari et al. [45] for efficient metal ion detection and organic dye catalysis.To boost MIL-125-NH_2's photocatalytic activity in dye degradation, Hossam E. Emam et al. [46] investigated doping it with silver tungstate and silver vanadate nanoparticles. Utilizing copper-supported WO_3 nanosheets for chemoselective, photocatalytic, and electrocatalytic applications were investigated by Farha Naaz and associates [47]. A simple co-precipitation technique was employed in this investigation to synthesize $CuWO_4$. The materials' structural features were provided by X-ray diffraction (XRD) and Raman Spectroscopy, while their composition was analyzed using Fourier transform infrared spectroscopy (FT-IR). The optical bandgap energies were estimated using UV-Vis spectroscopy and X-ray photoelectron spectroscopy (XPS) was employed to ascertain the binding energies at 284.8 eV with respect to C (1s). The Brunauer-Emmett-Teller (BET) analyses were used to determine the specific surface area.The elemental analysis was determined using Energy Dispersive Spectroscopy (EDS). The Photoluminescence Studies were also employed. Additionally, the chemocatalytic ability of the nanostructured $CuWO_4$ in breaking down organic contaminants was assessed.

Highlights

- $CuWO_4$ nanoparticles with enhanced catalytic degradation were synthesized using the co-precipitation method.
- The as-synthesized sample and the sample heat-treated at 300°C exhibit $CuWO_4$ nanoparticles with a monoclinic phase and a large surface area, which are essential for catalytic degradation.
- They demonstrate a catalytic degradation of nearly 98.3% for Methylene blue, indicating potential applications in wastewater management.

2. EXPERIMENTAL

Analytical-grade cupric chloride ($CuCl_2.H_2O$), sodium tungstate ($Na_2WO_4.H_2O$, 99%), methylene blue ($C_{16}H_{18}ClN_3S$, Nice) and acetone (99%) were directly employed without any extra purification. We utilized the deionized water as the solvent across the experiment, and all glassware was thoroughly rinsed.

2.1. Preparation techniques

Employing the simple co-precipitation technique, an aqueous solution of copper tungstate was reacted to create nanosized powder $CuCl_2.2H_2O$ (8.5 g) and $Na_2WO_4{\cdot}2H_2O$ (16.49 g) at ambient temperature with continuous stirring. Thereby produced blue precipitate was centrifuged to remove excess NaCl that had formed as a by-product, and it was then repeatedly filtered and cleaned with distilled water before being dried for two hours at 100°C in an air oven. The end product is calcinated at 300°C, 400°C, 500°C and 600°C for 2h each. The as-synthesised sample is coded as CW and the samples calcinated at 300°C,

400°C, 500°C, and 600°C were coded as CW1, CW2, CW3, and CW4 respectively.

2.2. Catalytic studies

The catalytic efficiency of the generated $CuWO_4$ nanostructure was assessed by tracking the color decay of the organic contaminant methylene blue (MB). 20 ml of 3.12 x 10^{-5} M dye solutions were mixed with 2 ml of 0.012 M powder catalyst to create the catalytic mixture. The reaction combination,1ml of 0.079 M $NaBH_4$ solution was introduced to make sure the reduction process. By monitoring the drop in absorbance at the wavelength that corresponds to the maximum absorption for MB dye in the UV-visible region as a function of time, in accordance with Beer's law, the break down reaction was tracked using a UV-visible spectrometer. The slow decline in absorbance over time illustrates the dye's decay deterioration rate was calculated by plotting measured absorbance against time. To determine the percentage of dye decline, the following formula was used:

$$Decolorization\ \% = \frac{C_0 - C}{C_0} \times 100\% \qquad (1)$$

Where C_0 is the initial MB level after adsorption and the desorption equilibrium is attained before radiation. C represents the contaminant concentration at different points in time after the catalytic reaction.

3. RESULTS AND DISCUSSIONS

3.1. X-ray diffraction analysis

The XRD patterns of the samples heat-treated at various temperatures, along with the as-synthesised samples, are displayed in **(Fig.1)**. The XRD patterns of the CW and CW1 samples **(Fig.1. a)** show a low degree of crystallinity. Broad peaks with low intensities were obtained around 2θ values at 11.8°, 22.3°, 29.6°, 35.7°, 40.4°, 53.2°, and 63.7°. The number and position of peaks in the XRD pattern of these samples were reported in the literature [48, 49] present a similar broad pattern assigned to $CuWO_4.2H_2O$ monoclinic structure, in reference to ICDD card No. 33-0503 [50]. Both the impacts of order-disorder transitions and the existence of water molecules bound in this crystalline structure may be liable for this broadening [51], i.e., these particles do not possess an extensive long-term structural arrangement. When the process of heat treatment was performed at temperatures 400 °C, 500 °C and 600 °C for 2 hours, water molecules in the $CuWO_4{\cdot}2H_2O$ were completely eliminated and the diffraction peaks appeared in XRD patterns attributed to $CuWO_4$ triclinic structure, in keeping with the ICDD card No. 01-072-0616 [52] with space group ($P\bar{1}$) [49].

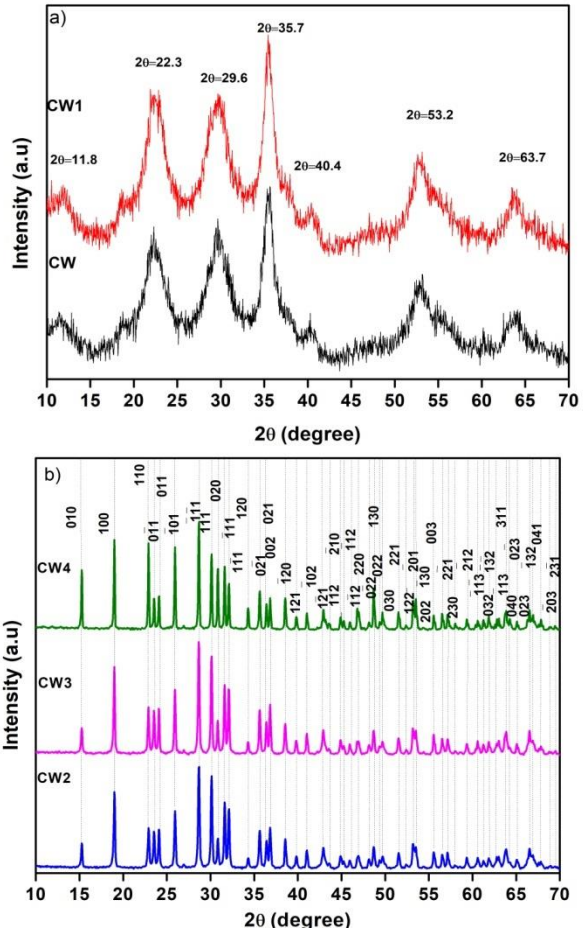

Figure 1. a) XRD pattern of the as-synthesised sample and the sample annealed at 300 °C b) the samples annealed at 400, 500 and 600°C.

From **(Fig.1.b)** the samples CW2, CW3, and CW4 show well defined peaks at 2θ values (lattice reflection planes)15.2° (010) 19° (100), 22.9° (110), 23.6° ($0\bar{1}1$), 24.1° (011), 26.9° (101), 28.7° ($\bar{1}\bar{1}1$), 30.1° (111), 30.8° (020), 31.6° ($\bar{1}11$), 32.1° ($1\bar{1}1$), 34.3° (120), 35.6° ($0\bar{2}1$), 36.4° (021), 36.8° (002), 38.6° ($\bar{1}20$), 39.8° (121), 41.0° ($\bar{1}02$), 42.9° ($1\bar{2}1$), 43.5° ($\bar{2}10$), 44.9° (112), 45.2° ($\bar{1}12$), 45.9° ($1\bar{1}2$), 46.8° (220), 48.1° ($0\bar{2}2$), 48.7° (130), 49.4° (022), 49.7° (030), 51.5° (221), 52.4° (122), 53.2° ($\bar{2}01$), 53.5° ($\bar{1}30$), 55.5° (202), 56.5° (003), 57.1° ($2\bar{2}1$), 58° (230), 59.2° ($2\bar{1}2$), 60.6° ($\bar{1}\bar{1}3$), 61.2° ($\bar{1}32$), 61.9° (032), 62.8° ($\bar{1}13$), 63.8° (311), 64.2° (040), 65.1° ($0\bar{2}3$), 66.6° (023), 67.0° ($\bar{1}32$), 67.9° (041), 69.0° ($\bar{2}03$), 69.7° ($21\bar{3}$). The XRD spectra showed no discernible peaks indicating impurities like copper oxide or tungsten oxide, and all of the peaks exactly matched the pure $CuWO_4$ phase, indicating that the triclinic phase of $CuWO_4$ was produced.

The following formula is used to get the mean size of the crystallite (D_{hkl}) across the various samples: Debye-Scherrer equation [53]

$$D_{hkl} = K\lambda / \beta_{hkl} cos\theta_{hkl} \quad (2)$$

where λ is the wavelength of the X-ray, *K* is the shape factor (0.90), θ_{hkl} is the Bragg diffraction angle, and β_{hkl} is the FWHM in radians of the main peak in the XRD pattern. The acquired results of crystalline size for CW, CW1, CW2, CW3& CW4 are approximately 5nm, 6nm, 57 nm, 60 nm, and 82 nm accordingly. The finer particles of CW and CW1 were converted to larger particles of CW2, CW3, and CW4 samples by increasing the calcination temperature. With the increase in temperature, water molecules from $CuWO_4.2H_2O$ were eliminated and the samples CW2, CW3, and CW4 attained reduced specific surface area, greater crystallinity, and increased crystallite size compared to $CuWO_4.2H_2O$ nanoparticles [54]. With increasing temperature, the intensity is found to increase, and the FWHM decreases. We have determined the mean values of each lattice parameter using the equation,

$$\frac{1}{d^2_{hkl}} = \frac{1}{V^2}[b^2c^2sin^2\alpha h^2 + a^2c^2sin^2\beta k^2 + a^2b^3sin^2\gamma l^2 + 2abc^2(cos\,\alpha\,cos\,\beta - cos\,\gamma)hk + 2a^2\,bc(cos\,\beta\,cos\,\gamma - cos\,\alpha)kl + 2ab^2c(cos\,\alpha\,cos\,\gamma - cos\,\beta)hl] \quad (3)$$

where *a, b* and *c* are the lattice parameters (*hkl*) are Miller indices, 'd_{hkl}' is interplanar distance and V is the volume, $V = abc\sqrt{1 - cos^2\alpha - cos^2\beta - cos^2\gamma + 2\cos\alpha\cos\beta\cos\gamma}$ [55]. Table 1 shows the values that have been determined which are consistent with the values provided in the ICDD CARD [52].

Table 1. Samples lattice parameter and mean crystallite size

Sample	Crystallite Size (nm)	Lattice parameter
CW	5	-
CW1	6	-
CW2	57	a=4.878, b=5.839, c= 4.703
CW3	60	a=4.878, b=5.839, c= 4.703
CW4	82	a=4.878, b=5.839, c= 4.703

3.2. Raman analysis

Raman spectroscopy is a popular non-destructive method for examining material characteristics, taking into account the chemical composition of the surface and the importance of oxygen vacancies in catalysis. As-synthesised and annealed samples' Raman spectra were shown in **(Fig. 2)**. 18 Raman-active vibrational modes are found in tungstates with triclinic structure, space group ($P\bar{1}$), and point group symmetry (C_i), according to group theory calculations. External and internal modes are the two categories into which vibrational modes found in tungstate Raman spectra are categorised, per the literature [48,81]. The Raman spectra of $CuWO_4$ can be interpreted in terms of internal and external modes of the WO_6 octahedra. The motion of rigid units and distorted octahedral [CuO_6] clusters (O_h symmetry) is associated with lattice phonons, which are related to the vibrational external modes. Assuming that the centre of mass is stationary, vibrational internal modes are attributed to vibrations of deformed octahedral [WO_6] clusters in the lattice. Point group symmetry (C_i) is present in distorted octahedral [WO_6] clusters, where internal modes (A_g) make up the vibrations while external modes (A_g) make up the remaining vibrations. The notch filter used to suppress the laser line and associated Rayleigh scattering may shut off the remaining modes, making it impossible to see the remaining sixteen modes. The observed modes are located at 96, 128, 180, 192, 223, 283, 293, 315, 355, 405, 479, 550, 733, 779, and 906 cm^{-1}. The stretching modes of $CuWO_4$ are those at 405, 550, 676, 733, 779, and 906 cm^{-1} [21]. 180, 192, 223, 283, 293, 315 and 355 cm^{-1} are attributed to the bending modes of $CuWO_4$. The Raman results show that the published Raman-active vibrational modes and our experimental ones agree well. Variations in the degree of structural order-disorder on both octahedral [CuO_6] and [WO_6] clusters can be linked to the slight displacements in the positions of these vibrational modes. This is because each synthesis condition (temperature, time) has unique characteristics. As observed from the figures there are Raman-active modes for $CuWO_4.2H_2O$ and $CuWO_4$. The samples which have vibrational modes arising from water molecules in $CuWO_4.2H_2O$ (the deconcovoluted **(fig (b) and (c))**, i.e, broad band at 90 and 130 cm^{-1} for CW and 90 cm^{-1} for CW1 indicate that they are not so crystalline.

The band corresponding to water molecule is absent in all other samples and got sharp Raman peaks for CW2, CW3 and CW4 meant that the $CuWO_4$ nanoparticles were well crystalline on increasing the annealing temperature in particular, the most prominent band at 906 cm^{-1} is thought to be the $CuWO_4$ phase's fingerprint. It's also crucial to keep in mind that the heat treatment produced stronger and more distinct Raman-active bands for $CuWO_4$. In this instance, the changes in

temperature also cause this oxide's short-range structural ordering to increase.

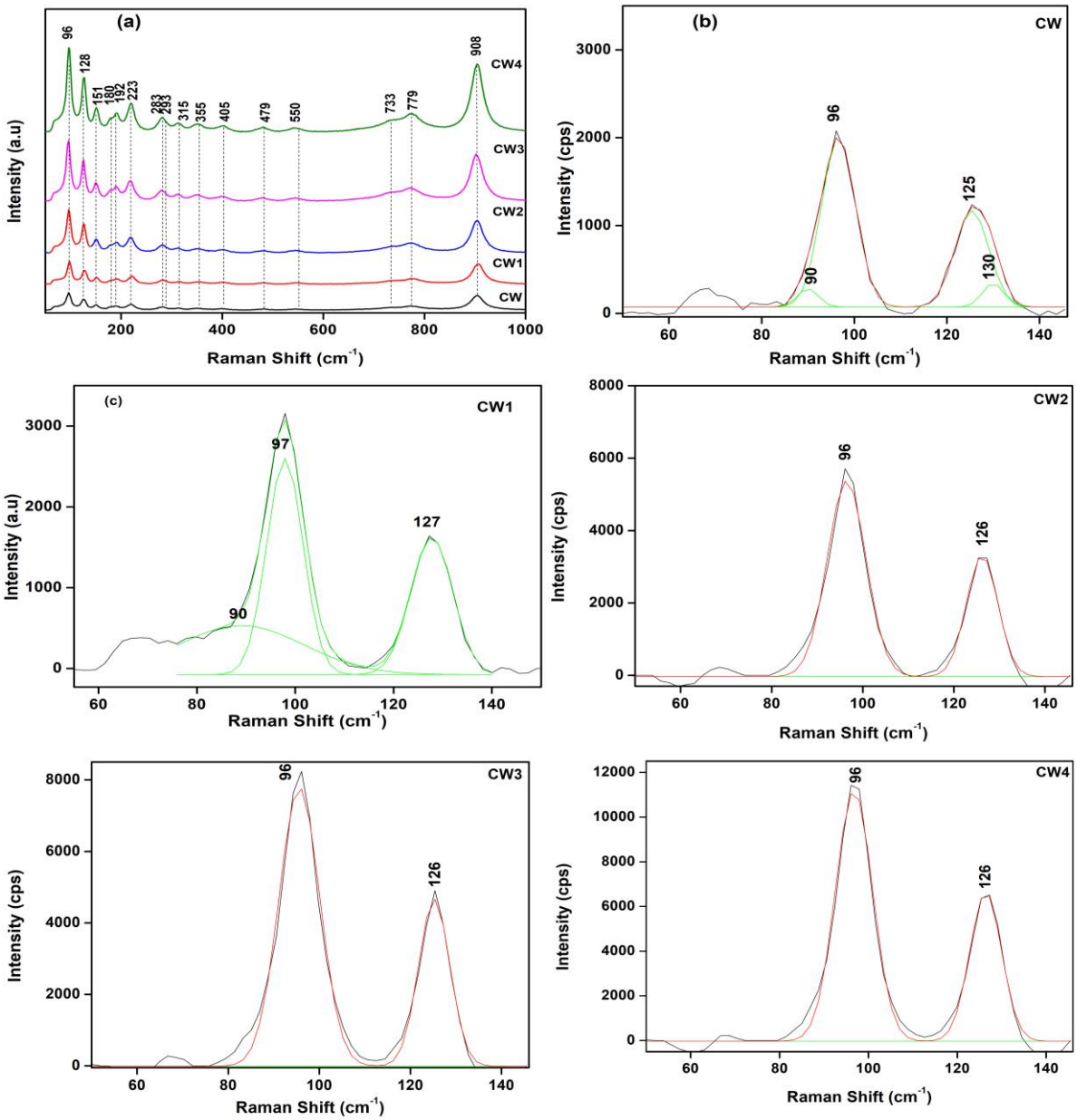

Figure 2. Raman spectra of as- synthesized and annealed $CuWO_4$ samples

3.3. FT- IR analysis

FT-IR spectroscopy was used to examine the formation of $CuWO_4$ and the detection of functional groups in the synthesised samples. The FT-IR spectra of both as-synthesised and annealed samples are displayed in (**Fig. 3**). The literature asserts that the nanostructured $CuWO_4$ has 18 IR-active vibrational modes and a triclinic structure [48]. As illustrated in (**Fig. 2**), We only found 12 IR-active vibrational bands [Au modes] in our infrared spectra. The explanation for this tendency is the complicated phonon pattern interrelated with every mode, which typically involves the entire unit cell, and the low symmetry of the $CuWO_4$ lattice. However, the primary atomic shifts provide give information about atomic dynamics related to the highest energy modes [56]. The FTIR spectra of CW and CW1 samples showed a wide infrared absorption band between 3300 and 3500 cm^{-1}, which is indicative of stretching vibrations of hydroxyl (OH) groups. This confirmed the presence of water molecules and a significant OH group in these materials [57]. Adsorbed water's -OH stretching and H-O-H bending vibrations are responsible for the band at 1631 cm^{-1} in these samples [58]. The 900–400 cm^{-1} range contained

the distinctive stretching absorption peaks of $CuWO_4$ compounds [59]. Five absorption bands are observed below 900 cm^{-1}which are linked to the vibrational and stretching bands of the $CuWO_4$ [60]. These peaks are consistent with previous observations that identified the 450–1000 cm^{-1} range of Wolframite-type structure AWO_4's principal absorption bands, where A = Fe, Ni, Mn, Cd, Mg, Zn, and Cu [61]. But the vibrational bands of the CuO_6 polyhedra are what cause the absorptions seen below 500 cm^{-1}. Cu–O band stretching is the cause of the absorption band that can be seen in the spectra at 601–800 cm^{-1}. Potential explanations for the absorption bands seen below 601 cm^{-1} include the deformation modes of W–O bonds in WO_4 tetrahedra or the deformation modes of W–O–W bridges [60, 61]. It was determined that the peak originated from the (–O–W–O–W–O–) symmetric stretching vibration among $[WO_6]$–$[WO_6]$ clusters in the FT-IR spectra located around 562 cm^{-1} [59,62]. As expected from Table 2, The IR-active vibrational modes observed in this study are consistent with previous research findings. $CuWO_4$ is thus formed as the outcome of the precipitation reaction, as demonstrated by the data in **(Fig. 3)**.

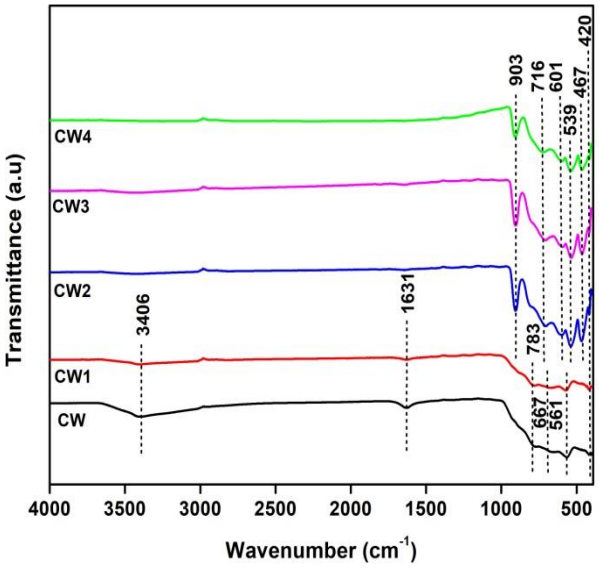

Figure 3. FTIR spectra of as-synthesised and annealed $CuWO_4$ samples in the range (400–4000 cm^{-1})

Table 2. FTIR of as-synthesised and annealed samples

Sample	CW	CW1	CW2	CW3	CW4	Assignment	Ref.
Wavenumber (u cm^{-1})	3406	3406	-	-	-	O-H, Stretching vibration.	[57]
	1631	1631	-	-	-	H–O–H Bending vibrations	[58]
	-	-	903	903	903	W–O Stretching mode	[60]
	783	783	-	-	-	Cu–O Stretching	[61]
	-	-	716	716	716	Cu–O Stretching vibration	[63]
	-	-	601	601	601	Cu–O Stretching mode	[60]
	561	561	-	-	-	(–O–W–O–W–O–) Stretching Vibration between $[WO_6]$–$[WO_6]$ clusters	[59]
	-	-	539	539	539	W–O Bonds deformation mode	[60]
	-	-	467	467	467	W – O– W Deformation bridging mode	[61]
	420.	420	420	420	420	(-O-W-O-) Symmetric bending vibrations in $[WO_6]$ clusters	[48]

3.4. UV diffuse reflectance studies

A straightforward and practical method for figuring out the band gap value is diffuse reflectance spectroscopy (E_g) (**Fig. 4a)**.displays the UV-Vis diffuse reflectance spectra of the samples.All of the nanostructured $CuWO_4$ spectra exhibit reflectance in the 350–800 nm wavelength range, as can be seen in this figure. However, the curves for the samples annealed at 400 °C, 500 °C, and 600 °C exhibit a broad band in the wavelength range of 400 nm to 800 nm, whereas the as-synthesised sample and the sample annealed at 300 °C show a λ_{max} reflectance at 555 nm and 570 nm, respectively. From the reflectivity data, the optical band gap energy (E_g) for the nanostructured $CuWO_4$ is computed using the Kubelka and Munk (KM) method [48, 64]. This method converts diffuse

reflectance measurements to provide a highly accurate estimation of semiconductor E_g values. [65].

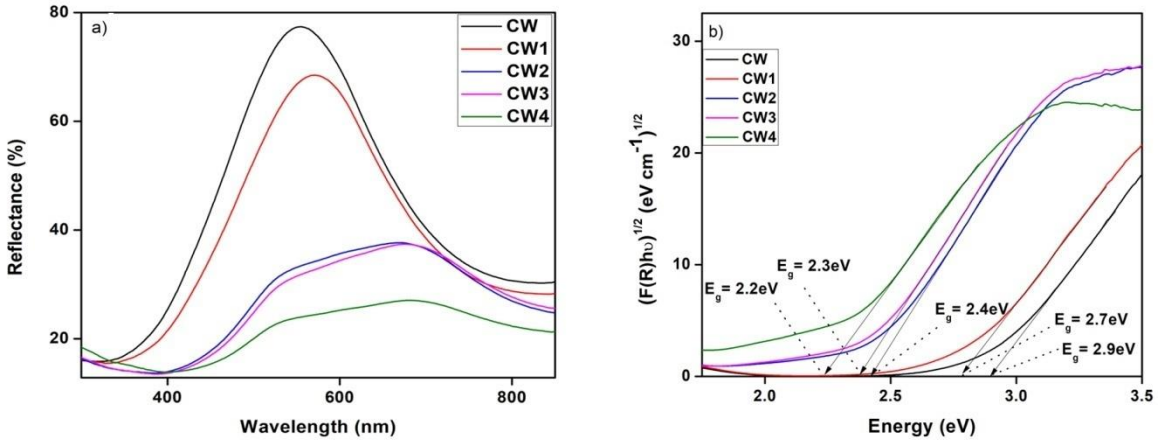

Figure 4. a) UV–Vis diffuse reflectance spectra of as-synthesized and annealed $CuWO_4$ samples, b) Band gap overlay spectrum of $CuWO_4$ samples (Kubelka- Munk plot).

One can use the KM function to determine the optical absorption edge energy for the diffused reflectance spectra, and the relation gives the equivalent absorption coefficient F(R) [64]:

$$F(R) = {}^{K}/_{S} \quad (4)$$

$$F(R) = \frac{(1-R)^2}{2R} \quad (5)$$

where K is the molar absorption coefficient, $K = (1-R)^2$, S is the scattering factor, $S=2R$, where R is the reflectance of the sample. The optical band gap of $CuWO_4$ can be determined using the indirect transition equation and F(R) as follows:

$$F(R)h\nu = A(h\nu - E_g)^n \quad (6)$$

where $h\nu$ is the photon energy, A is a constant, E_g is the band gap, $F(R)$represents the Kubelka-Munk function, and n is a constant related to the type of electronic transition (n = 0.5, 2, 1.5, and 3 for direct allowed, indirect allowed, direct forbidden, and indirect forbidden transitions, respectively).

Based on the literature [66] and [67], Through the process of electronic absorption, the electrons in the maximum-energy states in VB indirectly return to the minimum-energy levels in CB (different locations within the Brillouin zone). The electrons in the maximum-energy states in VB indirectly return to the minimum-energy states in CB (various places in the Brillouin zone) via the electronic absorption process. [68]. This data was used to compute the E_g values of $CuWO_4$ using n = 2 in Eq. (6).KM equation can be obtained, as indicated by

$$(F(R)h\nu)^{1/2} = A(h\nu - E_g) \quad (7)$$

The linear portion of the figure of$(F(R)h\nu)^{1/2}$ versus photon energy *hu* on the x-axis was extrapolated to determine the optical band E_g. As illustrated in Fig. 4b, the E_g values of samples exhibited a downward trend from 2.9 to 2.2 eV with the rise in heat treatment temperature. For the as-synthesised sample and the heat-treated sample heated to 300 °C, this trend was ascribed to the removal of water molecules (dehydration process) from the lattice, which caused a phase transition from $CuWO_4{\cdot}2H_2O$ to $CuWO_4$. Low symmetry and distortions in both the octahedral [CuO_6] and [WO_6] clusters in the lattice can account for the drop in E_g values for samples heated to 400 °C, 500 °C, and 600 °C, which corresponds to the $CuWO_4$ triclinic phase [48,64].

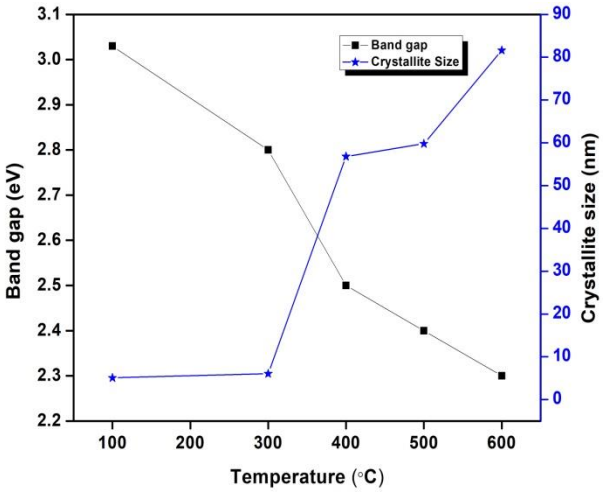

Figure 5. Variation of band gap and crystallite size with temperature.

Table 3. Variation of band gap and crystallite size with temperature.

Sample	Band GAP energy (E_g) eV	Crystallite size (nm)
CW	2.9	5

CW1	2.7	6
CW2	2.4	57
CW3	2.3	60
CW4	2.2	82

It has been noted that when temperature rises, the band gap reduces (Table 3), and the variation in band gap energies of the samples aligns with the variation in crystallite size **(Fig.5)**.

The samples' quantum confinement effect may be the cause of this behavior. The band gap and absorption edge of nanostructured materials change due to quantum size effects (QSE) [69].

3.5. BET surface area analysis

The surface area of the samples was ascertained by N_2 physisorption, and the N_2 adsorption/desorption isotherms are shown in (**Fig. 6)**

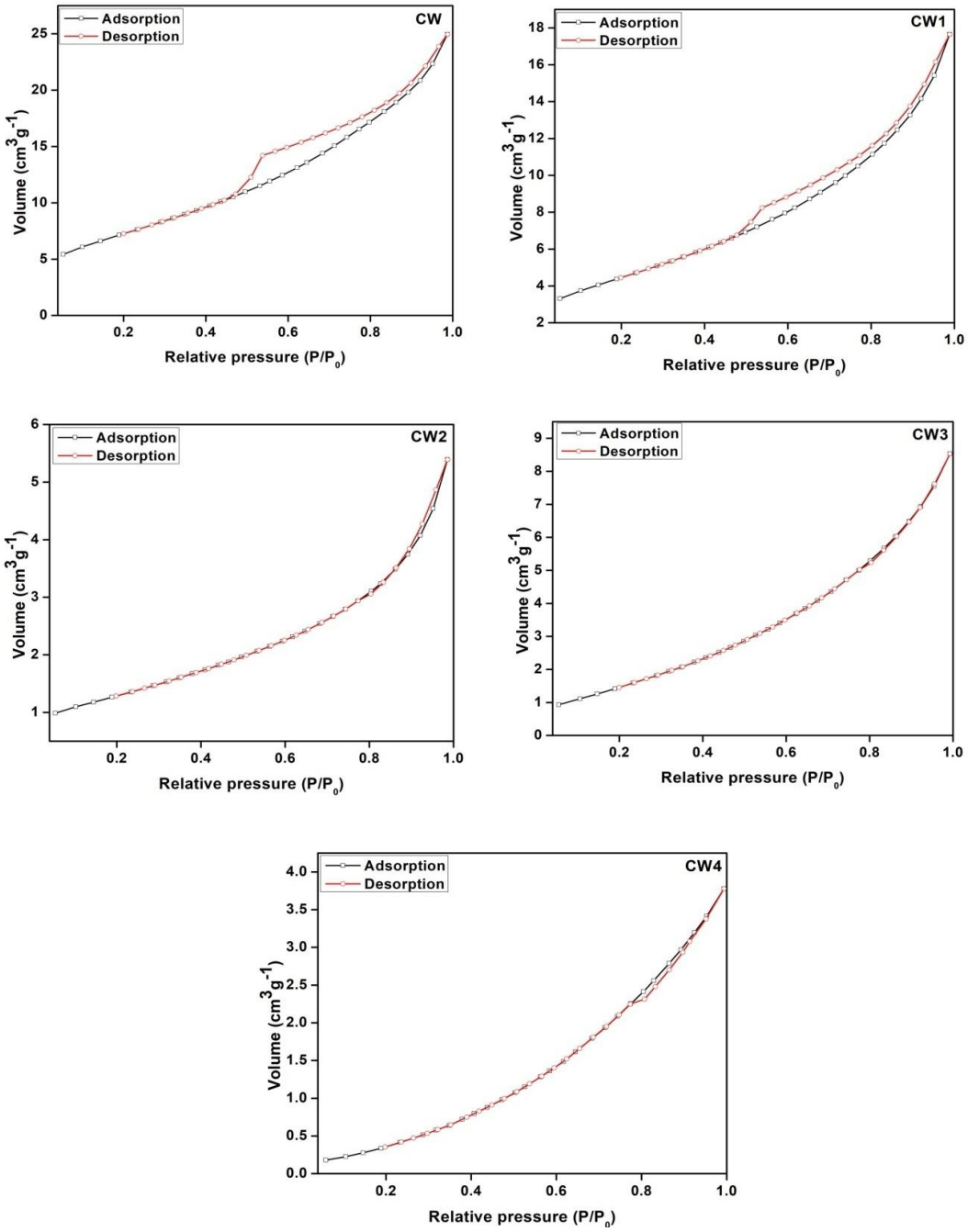

Figure 6. Nitrogen adsorption—desorption isotherm of the $CuWO_4$ samples

The BET surface areas, pore volumes, and pore sizes of the synthesized samples are summarized in Table 4. Surface areas of 26.28, 16.24, 4.64, 5.06, and 2.03 m^2/g were measured for CW, CW1, CW2, CW3, and CW4 respectively. This pattern fits in nicely with variations in the average crystallite sizes determined by XRD. The samples CW and CW1 exhibit large surface areas compared to other samples, which prompted further investigation into their catalytic activity. The smaller surface areas obtained for CW2, CW3, and CW4 samples are possibly due to grain growth during heat treatment at higher temperatures. This characteristicis expected to pose challenges in the catalytic evaluation of these samples. The IUPAC categorization states that N_2 adsorption/desorption isotherms are type IV with an H3 hysteresis loop [54]. The hysteresis loopof CW is larger compared to the other samples. As the sintering temperature rises, average pore size of the samples grows while their surface area falls.

Table 4. BET surface area, pore volume, and pore size of the $CuWO_4$ samples.

Sample	Surface area (m^2/g)	Pore volume (cm^3/g)	Pore size (NM)
CW	26.28	0.039	5.87
CW1	16.24	0.027	6.72
CW2	4.64	0.008	7.18
CW3	5.06	0.013	8.62
CW4	2.03	0.060	11.35

3.6. X-ray photoelectron spectroscopy

The elemental and surface content of samples made using the co-precipitation method were examined using X-ray photoelectron spectroscopy (XPS) studies, as illustrated in **(Fig. 7)**. Fig. 7a displays the complete survey spectrum, which shows the presence of Cu2p, O1s, and W4f states confirming the presence these elements in $CuWO_4$ samples [70].To calibrate the binding energy scale, the adventitious carbon C 1s peak, which is located at 284.8 eV, was utilized [71]. Carbon adsorbed on the surface of the AWO_4 samples is responsible for this peak,likely resulting from incomplete removal of polymeric precursors during thermal treatment [72]. **(Fig. 7b**) exhibits peaks at binding energy values 955.5-954.4 eV ($Cu2p_{1/2}$) and 935.5- 934.4 eV ($Cu2p_{3/2}$) corresponding to the oxidation state Cu^{2+} in the lattice sites of $CuWO_4$ [71]. In **(Fig.7c**). the samples CW and CW1 exhibit peaks at energy values 39/39.2 eV ($W5p_{3/2}$), 37.6/35.5 eV ($W4f_{5/2}$), and 35.5/35.4 eV ($W4f_{7/2}$) corresponding to the standard values of W^{6+} oxidation state [71] whereas for samples CW2, CW3, and CW4, the peaks were obtained at energy values 40.8/39.1/ 39.8/40.6 eV ($W5p_{3/2}$), 37.7/37.3/36.5 eV ($W4f_{5/2}$), and 35.9/34.6/35.5/34.5 eV ($W4f_{7/2}$). All of the samples in Fig. 7d show peaks at 530.5-530.1 eV, which correspond to the Cu-O-Cu bond's lattice oxygen, 532.2-531.4 eV corresponding to metal oxide Cu-O bond and 529.7 eV attributed to O-W-O bond [70].

Table 5. Binding energies of the $CuWO_4$ samples.

Binding energy(eV) Samples	O1s	W4f			Cu2p		Satellite peak
		$W4f_{5/2}$	$W4f_{7/2}$	$W5p_{3/2}$	$Cu(2p_{1/2})$	$Cu(2p_{3/2})$	
CW	530.5, 531.4	37.6	35.5	39	955.4	935.5	963.1, 944.7, 942.4
CW1	530.5, 531.6	37.4	35.4	39.2	955.4	935.5	962.8, 944.5, 942.3
CW2	530.9, 531.6, 529.7	37.7	35.9, 34.6	40.8	954.5	934.6	962.2, 944, 941.7
CW3	530.5, 531.6, 532.2	37.3	35.5	39.1, 39.8	955.4	935.5	963.1, 944.8, 942.6
CW4	530.1, 531.6	36.5	34.5	40.6	954.4	934.5	962, 943.7, 941.5

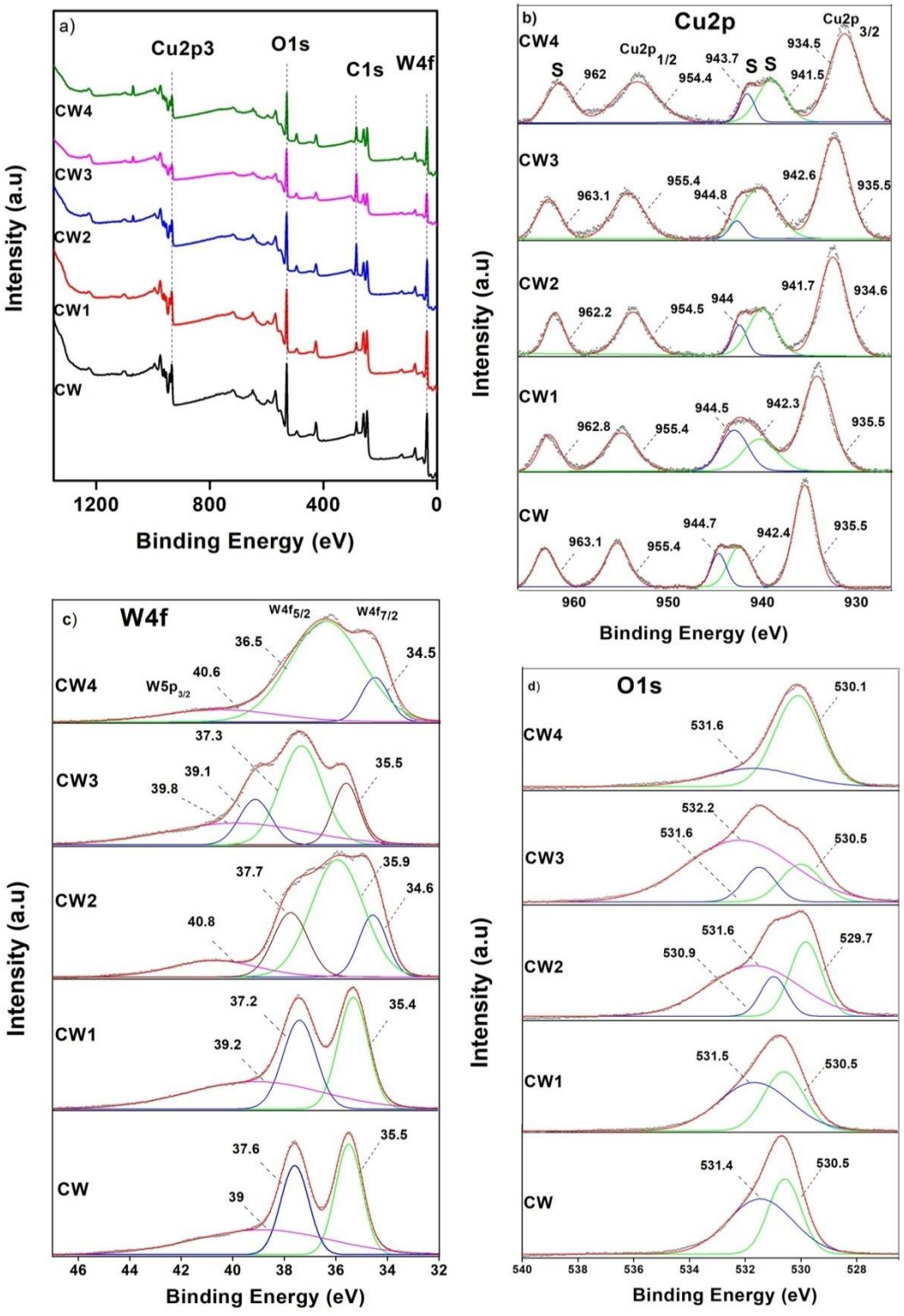

Figure 7. XPS (a) survey spectra, (b) Cu 2p, (c) W 4f, and (d) O1s peaks for the $CuWO_4$

3.7. EDS analysis

The elemental measurements recorded by energy-dispersive spectroscopy EDS analysis is shown in **(Fig. 8**) confirmed the presence of Cu, W, and O elements, indicating the synthesis of $CuWO_4$. It is clear from the table 6, Oxygen content decreases with increase in annealing temperature. This decrease in atomic weight percentage of oxygen can be due to the transformation of $CuWO_4.2H_2O$ to $CuWO_4$. Increase in W content

can de due to the crystallization of $CuWO_4$. For samples CW and CW1, $CuWO_4.2H_2O$ is present and for the samples CW2, CW3 and CW4, $CuWO_4$ phase is present. This is in well agreement with the results of XRD and Raman analysis.

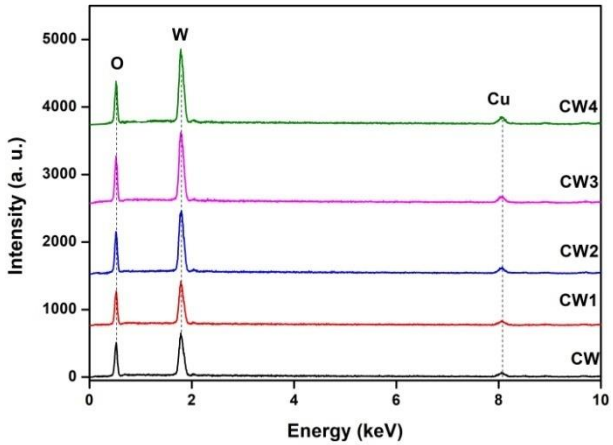

Figure 8. EDS spectra of as-synthesized and annealed $CuWO_4$ samples

Table 6. Elemental measurements of the samples

Samples	Atomic Wt %			Total
	W	O	Cu	
CW	9.83	68.87	21.29	100
CW1	10.57	67.40	22.03	100
CW2	11.49	66.75	21.76	100
CW3	11.51	66.45	22.04	100
CW4	12.27	61.05	26.68	100

3.8. Photoluminescence studies

Photoluminescence (PL) spectra of as-synthesised and heat-treated samples at different temperatures with an excitation wavelength of 290nm are shown in (**Fig. 9)**. The emissions appeared at wavelengths between 400 and 500 nm for all the samples. In our work, the deformed octahedral [WO_6] clusters are assumed to have a significant role in the electronic transitions involving the energy levels between the VB and CB. The existence of interconnections between octahedral [WO_6] and [CuO_6] clusters in the triclinic lattice indicates that any distortion caused on [WO_6] clusters also promotes a slight deformation on O–Cu–O bonds [CuO_6] clusters. O–Cu–O bonds exhibit a significant degree of distortion because they are covalent rather than ionic. The emergence of intermediate levels within the band gap can result from this Jahn-Teller effect along the z-axis, which can cause a symmetry break in the lattice [48]. From the figure, the intensity of PL for as-synthesised and heat-treated samples at 300 °C is correlated to the progressive elimination of water molecules from $CuWO_4.2H_2O$ samples. As in the literature [48] we also found a quenching or significant reduction in the PL intensity for $CuWO_4$ samples, i.e., for samples heat treated at 400 °C, 500 °C and 600 °C respectively. Also, it was noted a change in the color of the powders from light green to dark. According to black body theory, a hypothetical material (black) absorbs all the electromagnetic radiation. Therefore, the laser employed in the excitation process was more absorbed and not reflected in PL measurements of $CuWO_4$ samples [48].

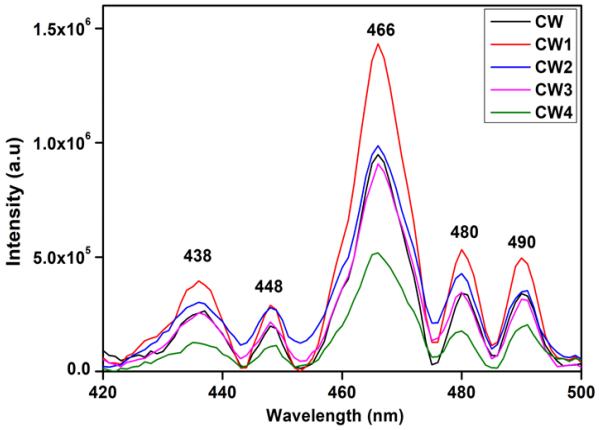

Figure 9. PL spectra of as-synthesized and annealed $CuWO_4$ samples

3.9. Catalytic study

There are significant worries about the detrimental effects on the environment of liquid or gaseous effluents produced by factories, labs, and other industries. Textile and industrial dyes, which are frequently lost during the coloring process, are among the most important categories of organic pollutants [73, 74]. The color contaminants cannot be effectively removed by typical methods such adsorption, ion exchange on synthetic adsorbent resins, chemical agent coagulation, reverse osmosis, and ultrafiltration due to their temperature constancy. Nevertheless, because of their advantageous band gap energy and electrical structure, semiconductor nanoparticles have been shown to function as catalysts in photo-induced processes [75, 76]. The hazardous organic pollutant MB was reduced using $NaBH_4$ as the reducing agent in all conditions to evaluate the chemocatalytic effectiveness of $CuWO_4$ nanostructures. UV-vis spectrophotometer was used to track the reduction reaction. Because of its toxicity, MB, a common heterocyclic aromatic dye in the textile industry, presents serious environmental problems. When MB is in its oxidized state, it has two distinct absorption bands in the visible spectrum. Around 612 nm, the shoulder band is linked to the formation of dimer $(MB)^2$ in an aqueous solution, while the main band at about 665 nm is caused by n-π* transitions [77]. Reduction of MB with $NaBH_4$ produces colourless leucomethylene blue [78].

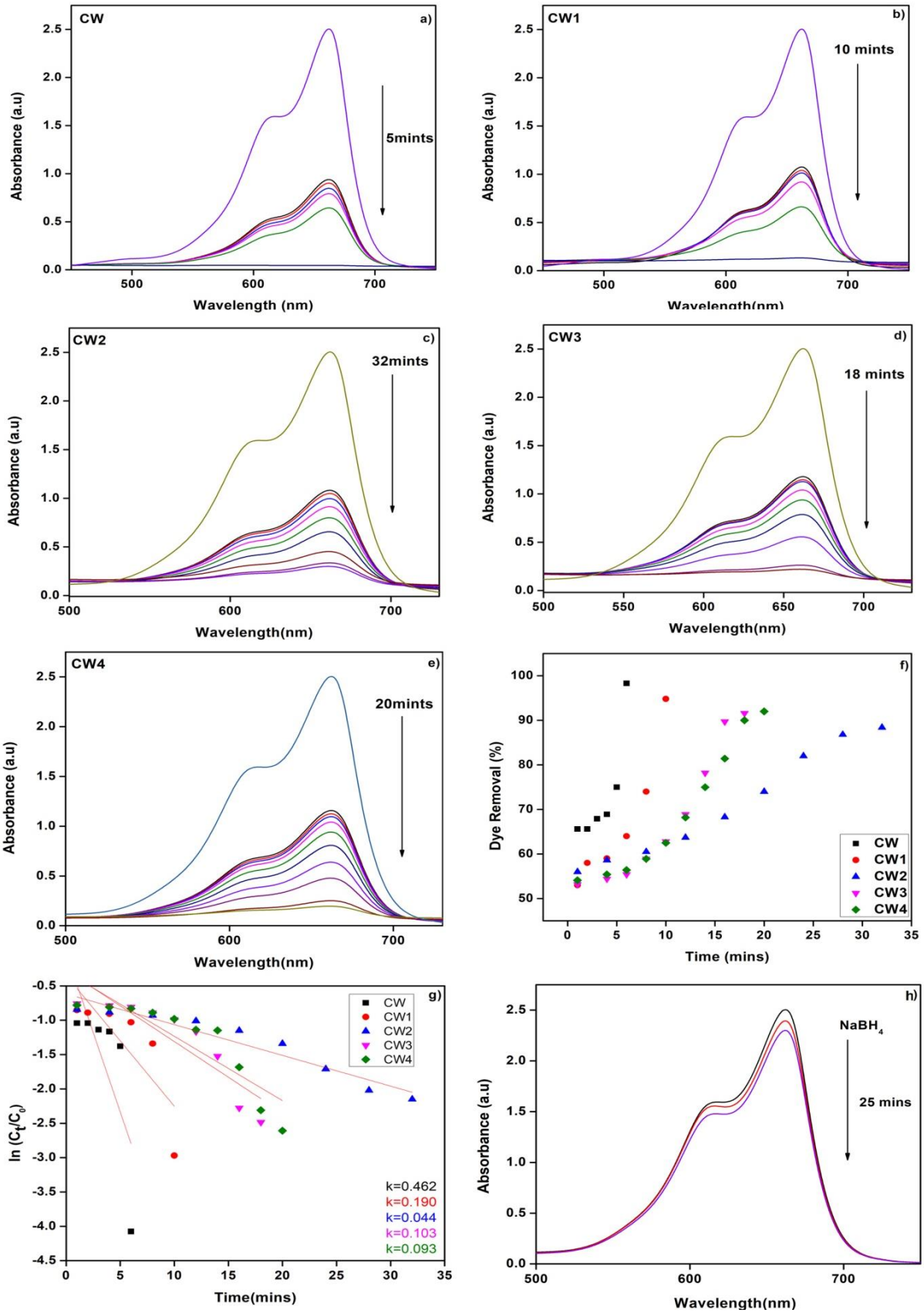

Figure 10. a-e) UV–Visible absorbance spectrum of a methylene blue, f) percentage of dye degradation, g) Time profiles of ln (C_t/C_0) h) UV-Vis absorbance spectrum of $NaBH_4$.

The linear plot of $ln[C/C_0]$ against reaction time (t), where C_0 is the initial MB concentration after adsorption and C is the concentration of pollutants at different times (Fig.10g), was used to determine the pseudo-first-order reaction rate constant (k) for the pseudo-first-order reduction reaction. The slope of the linear plot corresponds to k as revealed from the equation,

$$ln[\boldsymbol{C}/\boldsymbol{C_0}] = -kt \quad (8)$$

The k value, percentage degradation and the regression coefficient (R^2) for each linear fit are given in Table 7. The (eq.1) is used to determine the reactions' percentage degradation ($\%D$) [63].

In the absence of a catalyst, a study with the reducing agent $NaBH_4$ was carried out to evaluate the catalyst's contribution to the degrading process. As shown in **Fig.10h**, the degradation is minimal without $CuWO_4$ despite of the thermodynamic favourability of the reaction. However, upon the addition of $CuWO_4$ as a catalyst, the dye's color progressively faded and the adsorption intensity gradually dropped, indicating significant reduction of MB. The degradation times for samples CW, CW1, CW2, CW3, and CW4 were 5, 10, 32, 18, and 20 minutes, as depicted in (**Fig.10a-10e)**. The samples CW and CW1 exhibited superior catalytic performance consistent with their smaller crystallite size as revealed by the XRD analysis. The larger surface-active sites, as shown by BET measurements, and the smaller crystallite size of the produced $CuWO_4$ NPs are responsible for the increased catalytic activity. Plots of the % degradation against the reaction time are displayed in (**Fig. 10f)** to compare the catalytic performance of the samples across several degradation reactions. The MB breakdown and leucomethylene blue generation are confirmed by the absorption band's weakening and broadening. The suppression of the absorption band indicates a considerable acceleration of the reduction process upon the addition of $CuWO_4$ nanocatalyst. Furthermore, when the ratio of absorbance is plotted against time (**Fig.10a-10e**), according to the findings, the dye removal procedure is unaffected by the $NaBH_4$ concentration based on the calculated degradation rates and dye concentration.

Hang et al. [59] under dark condition observed that the absorption efficiency of $CuWO_4$ for the antibiotic tetracycline has 36.7 % for the annealed samples at 300 °C and it gradually decreases with increase in annealing temperature. We have obtained a maximum catalytic degradation for the dye (MB) for the sample CW. It gradually decreases with increasing annealing temperature. Hang et al. have obtained optimum photocatalytic efficiency for $CuWO_4$ when it is calcined at 500 °C. In the case of photocatalysis the photon incident on the $CuWO_4$ materials induces electron – hole pairs. This electron – hole pair accelerates the degradation process of dye. In the case of chemocatalysis the role of photon is done by $NaBH_4$. The degradation of dye in the presence of catalyst can be enhanced by decreasing the kinetic barrier and by increasing the encounter probability.

One explanation for the decline in $CuWO_4$ NPs' presence is the redox potential of the donor and acceptor systems in the aqueous solutions. The redox reaction between the borohydrate ion (BH^{4-}) and the corresponding dyes plays a crucial role during the degradation process. Specifically, the nucleophilic BH^{4-} ion contributes an electron, while the electrophilic dye or dye precursor accepts it. Since the donor and acceptor have a high kinetic barrier, spontaneous reaction is uncommon and the reaction proceeds very slowly in the absence of a catalyst. The $CuWO_4$ catalyst efficiently gets past this obstacle by promoting and quickening the donor-acceptor atom reaction, which is connected to the intermediate redox potential. This catalytic activity is further enhanced by the electron relay effect, where $CuWO_4$ nanoparticles mediate the electron transfer bringing the reaction time down to a few minutes from several days. Electrostatic force causes reactant molecules to be adsorbed onto the $CuWO_4$ nanoparticle surface enhancing the degradation process [79,80].

Table 7. The time, R^2 value of the linear fit of the kinetic plots for degradation for the dyes, rate constants (k), and the percentage of dye degradation (%D).

Pollutant	Sample	Time (min)	R^2	Rate constant $k\times10^{-3}$ (min^{-1})	%D
Methylene Blue	CW	5	0.401	0.462	98.3
	CW1	10	0.565	0.190	94.8
	CW2	32	0.909	0.044	88.4
	CW3	18	0.765	0.103	91.6
	CW4	20	0.752	0.093	92

4. CONCLUSION

The $CuWO_4$nanoparticles were synthesised via simple co-precipitation method then by heat treatment at various temperatures. All of the samples were characterized by XRD, RAMAN, FT-IR, UV-DRS, XPS, BET, EDS and PL analysis in order to better understand their structural, optical and surface properties. The catalytical activity of as-synthesised and annealed samples were studied using optical absorption studies. The XRD and RAMAN analysis revealed the presence of monoclinic $CuWO_4$. $2H_2O$ in the as-synthesised

(CW) and heated up sample at 300 °C (CW1) whereas all other samples heat-treated at higher temperatures (CW2, CW3, and CW4) exhibit triclinic $CuWO_4$ structures with space group ($P\bar{1}$). FT-IR spectroscopy identified the corresponding functional groups, detecting the twelve IR-active vibrational modes in the $CuWO_4$ particles. UV-DRS analysis revealed that the particles exhibited absorbance in the visible region with band gap energies (E_{gap}) ranging from 2.9 to 2.2 eV. As the temperature rose, the E_{gap} values decreased, which was explained by the decrease in intermediate energy levels between the conduction band (CB) and valence band (VB). XPS analysis identified the electronic configurations and peak positions corresponding to W, O, and Cu. The BET surface analysis shows large surface areas in the samples CW and CW1 whereas smaller surface areas for samples CW2, CW3 and CW4. The EDS study confirmed the presence of Cu, W, and O elements in the samples. Photoluminescence (PL) study of as-synthesised and heat-treated samples at different temperatures with an excitation wavelength of 290 nm reveals that for all the samples the emissions appeared at wavelengths between 400 and 500 nm. The sample heat treated at 300 °C exhibited the highest PL emission at room temperature. The chemocatalytic efficiency of $CuWO_4$ nanostructures was assessed by reducing methylene blue (MB) using $NaBH_4$ as the reducing agent. The degradation is minimal without $CuWO_4$ while the adsorption intensity gradually decreased, and the dye's colour gradually faded with the addition of $CuWO_4$ nanoparticles. A significant reduction of MB is obtained for samples CW and CW1 compared to other samples showing their best suitability for catalytic reduction applications. This synthesis of $CuWO_4$ nanocatalysts, exhibiting excellent catalytic performance for MB degradation offers a promising solution for wastewater management applications.

Acknowledgements

The authors would like to thank CLIF, University of Kerala and Department of Physics St. Thomas College Thrissur for instrumentation support.

5. REFERENCES

[1] M. Sihvonen, S. Pihlainen, T. Y. Lai, T. Salo (2021) Crop production, water pollution, or climate change mitigation—Which drives socially optimal fertilization management most, Agricultural Systems, 186, 102985. https://doi.org/10.1016/j.agsy.2020.102985

[2] K. Shirvanimoghaddam, B. Motamed, S. Ramakrishna, M. Naebe (2020) Death by waste: Fashion and textile circular economy case, Science of the Total Environment, 718, 137317. https://doi.org/10.1016/j.scitotenv.2020.137317

[3] L. Xiao, J. Liu, J. Ge, (2021) Dynamic game in agriculture and industry cross-sectoral water pollution governance in developing countries, Agricultural Water Management, 243, 106417. https://doi.org/10.1016/j.agwat.2020.106417

[4] W.J. Youngblood, S.H.A. Lee, K. Maeda, T.E. Mallouk (2009) Visible light water splitting using dye-sensitized oxide semiconductors, Accounts of Chemical Research,42,9002398. https://doi:10.1021/ar9002398

[5] K. Qi, Zh. Li, Ch. Zhang, X. Tan, Ch. Wan, X. Liu, L. Wang, L.Duu-Jong (2020) Biodegradation of real industrial wastewater containing ethylene glycol by using aerobic granular sludge in a continuous-flow reactor: Performance and resistance mechanism, Biochemical Engineering Journal, 161, 107711. https://doi.org/10.1016/j.bej.2020.107711

[6] T.N. Edison, R. Atchudan, M.G. Sethuraman, Y.R. Lee (2016) Reductive-degradation of carcinogenic azo dyes using Anacardium occidentale testa derived silver nanoparticles, Journal of Photochemistry & Photobiology, B: Biology, 162,604–610. http://dx.doi.org/10.1016/j.jphotobiol.2016.07.040

[7] N. Manavi, A.S. Kazemi, B. Bonakdarpour (2017) The development of aerobic granules from conventional activated sludge under anaerobic-aerobic cycles and their adaptation for treatment of dyeing wastewater, Chemical Engineering Journal, 312,375–384. http://dx.doi.org/10.1016/j.cej.2016.11.155

[8] X. Xie, M. Liu, C. Wang, L. Chen, J. Xu, Y. Cheng, H. Dong, F. Lu, W.H. Wang, H. Liu (2016) Efficient photo-degradation of dyes using $CuWO_4$ nanoparticles with electron sacrificial agents: a combination of experimental and theoretical exploration, RSC Advances,6, 953-959. https://doi:10.1039/C5RA18788E

[9] R.P. Schwarzenbach, B.I. Escher, K. Fenner, T.B. Hofstetter, C.A. Johnson, U. Von Gunten, B. Wehrli (2006) The challenge of micropollutants in aquatic systems, Science,313, 1072. https://doi:10.1126/science.1127291

[10] U.M Garcia-Perez, A. Martinez-de la Cruz, J. Peral (2012) Transition metal tungstates synthesized by co-precipitation method: Basic photocatalytic properties, Electrochimica Acta, 81,227– 232. http://dx.doi.org/10.1016/j.electacta.2012.07.045

[11] P. Chen, H. Y. He (2014) H_2 evolution from H_2O/ H_2O_2/MWO_4 (M = Fe^{2+}, Co^{2+}, Ni^{2+}) systems by photocatalytic reaction, Res Chem Intermed, 40,1947–1956. https://doi:10.1007/s11164-013-1092-5

[12] X.A. L´opez, A.F. Fuentes, M.M. Zaragoza, J.A.D. Guill´en, J.S. Guti´errez, Ortiz, A.L, V. Collins-Martínez (2016) Synthesis, characterization and photocatalytic evaluation of MWO_4 (M= Ni, Co, Cu and Mn) tungstates, International Journal of Hydrogen Energy, 41,23312-23317. https://doi.org/10.1016/j.ijhydene.2016.10.117

[13] M. Pourmortazavia, M. Nasrabadib, M. Shalamzarib, M. Zahedic, S.S. Hajimirsadeghic, I. Omranib (2012) Synthesis, structure characterization and catalytic activity of nickel

tungstate nanoparticles, Applied Surface Science, 263,745–752. http://dx.doi.org/10.1016/j.apsusc.2012.09.153

[14] J. Ruiz-Fuertes, A. Friedrich, J. Pellicer-Porres, D. Errandonea, A. Segura, W. Morgenroth, E. Haussuhl, C.Y. Tu, A. Polian (2011) Structure solution of the high-pressure phase of $CuWO_4$ and evolution of the Jahn-Teller distortion, Chemistry of Materials, 23, 4220–4226. http://dx.doi.org/10.1021/cm201592h

[15] J. Ke, M. A. Younis, Y. Kong, H. Zhou, J. Liu, L. Lei, Y. Hou (2018) Nanostructured ternary metal tungstate-based photocatalysts for environmental purification and solar water splitting: a review, Nano-Micro Letters 10, 69. https://doi.org/10.1007/s40820-018-0222-4

[16] D. Errandonea, J. Ruiz-Fuertes (2018) A brief review of the effects of pressure on wolframite-type oxides, Crystals,8,71. https://doi:10.3390/cryst8020071

[17] N. Gaillard, Y. Chang, A. DeAngelis, S. Higgins, A. Braun (2013) A nanocomposite photoelectrode made of 2.2 eV band gap copper tungstate ($CuWO_4$) and multi-wall carbon nanotubes for solar-assisted water splitting, International Journal of Hydrogen Energy, 38,3166-3176. http://dx.doi.org/10.1016/j.ijhydene.2012.12.104

[18] M. Shekofteh-Gohari, A. Habibi-Yangjeh (2016) Fabrication of novel magnetically separable visible-light-driven photocatalysts through photo sensitization of Fe_3O_4/ ZnO with $CuWO_4$, Journal of Industrial and Engineering Chemistry, 44,174-184.http://dx.doi.org/doi:10.1016/j.jiec.2016.08.028

[19] A.E.B. Lima, M.J.S. Costa, R.S. Santos, N.C. Batista, L.S. Cavalcante, E. Longo, G.E. Luz Jr. (2017) Facile preparation of $CuWO_4$ porous films and their photoelectrochemical properties, Electrochimica Acta, 256,139–145. https://doi.org/10.1016/j.electacta.2017.10.010

[20] D. Errandonea, F. J. Manjon (2008) Pressure effects on the structural and electronic properties of ABX_4 scintillating crystals, Progress in Materials Science, 53,711–773. http://doi:10.1016/j.pmatsci.2008.02.001

[21] J. Ruiz-Fuertes, D. Errandonea, A. Segura, F.J. Manjon, Zh. Zhu, C.Y. Tu (2008) Growth, characterization, and high-pressure optical studies of $CuWO_4$, High Pressure Research, 28,565–570. http://dx.doi.org/10.1080/08957950802446643

[22] W. Ding, X. Wu, Q. Lu (2019) Structure and photocatalytic activity of thin-walled $CuWO_4$ nanotubes: an experimental and DFT study, Materials Letters, 253,323–326. https://doi.org/10.1016/j.matlet.2019.06.109

[23] B. Mohanty, K.K. Naik, S. Sahoo, B. Jena, B. Chakraborty, C.S. Rout, B.K. Jena (2018) Efficient photoelectrocatalytic activity of $CuWO_4$ nanoplates towards the oxidation of NADH driven in visible light, Chemistry Select. http://doi:10.1002/slct.201801137

[24] M. Zhou, Z. Liu, X. Li, Z. Liu (2018) Promising three-dimensional flowerlike $CuWO_4$ photoanode modified with CdS and FeOH for efficient photoelectrochemical water splitting, Industrial & Engineering Chemistry Research,57. http://doi:10.1021/acs.iecr.8b00358

[25] M.V. Lalic, Z.S. Popovic´, F.R. Vukajlovic´ (2012) Electronic structure and optical properties of $CuWO_4$: AN ab initio study, Computational Materials Science, 63,163–167. http://dx.doi.org/10.1016/j.commatsci.2012.05.074

[26] C.M. Gonzalez, X. Du, J.L. Dunford, M.L(2012) Post Copper tungstate thin-films for nitric oxide sensing, Sensors and Actuators B: Chemical 173,169‑176. https://doi.org/10.1016/j.snb.2012.06.067

[27] S. Poovaragan, R. Sundaram, C.M. Magdalane, K. Kaviyarasu, M. Maaza (2019) Photocatalytic activity and humidity sensor studies of magnetically reusable $FeWO_4$‑WO_3 composite nanoparticle, Journal of Nanoscience and Nanotechnology 19,859‑866.https://doi:10.1166/jnn.2019.15565

[28] P. Lannelongue, S. Le Vot, O. Fontaine, T. Brousse, F.Favier (2019) Electrochemical study of asymmetric aqueous supercapacitors based on high density oxides: C/$Ba_{0.5}$ $Sr_{0.5}$ $Co_{0.8}$ $Fe_{0.2}$ $O_{3-\delta}$ and $FeWO_4$/ $Ba_{0.5}$ $Sr_{0.5}$ $Co_{0.8}$ $Fe_{0.2}O_{3-\delta}$, Electrochimica Acta 326, 134886. https://doi.org/10.1016/j.electacta.2019.134886

[29] R.D. Kumar, S. Karuppuchamy (2014) Microwave-assisted synthesis of copper tungstate nanopowder for supercapacitor applications, Ceramics International, 40, 12397‑12402. http://dx.doi.org/10.1016/j.ceramint.2014.04.090

[30] R.D. Kumar, S. Karuppuchamy (2016) Microwave mediated synthesis of nanostructured Co‑WO_3 and $CoWO_4$ for supercapacitor applications, Journal of Alloys and Compounds, 674, 384‑391. https://doi10.1016/j.jallcom.2016.03.074

[31] C.L. Li, Z.W. Fu (2008) Nano-sized copper tungstate thin films as positive electrodes for rechargeable Li batteries, Electrochimica Acta 53,4293–4301. https://doi:10.1016/j.electacta.2008.01.014

[32] J. Liu, Z. Zhang, Z. Wang, M. Tang, J. Li, J. Yi, T. Zuo, Y. Wu, Q. Ma, (2017) Flower-like WO3/CoWO4/Co nanostructures as high-performance anode for lithium-ion batteries, Journal of Alloys and Compounds, 113,727107. https://doi.org/10.1016/j.jallcom.2017.08.057

[33] T. Peng, C. Liu, X. Hou, Z. Zhang, C. Wang, H. Yan, Y. Lu, X. Liu, Y.Luo (2017) Control growth of mesoporous nickel tungstate nanofiber and its application as anode material for lithium-ion batteries, Electrochimica Acta,224,460‑467. http://dx.doi.org/doi:10.1016/j.electacta.2016.11.154

[34] W. Thongpan, D. Louloudakis, P. Pooseekheaw, T. Kumpika, E. Kantarak, W. Sroila, A. Panthawan, W. Thongsuwan, P. Singjai (2019) Porous $CuWO_4$/WO_3 composite films with improved electrochromic properties prepared by sparking method, Materials Letters,257,126747. https://doi.org/10.1016/j.matlet.2019.126747

[35] Y. Tang, N. Rong, F. Liu, M. Chu, H. Dong, Y. Zhang, P. Xiao (2016) Enhancement of the photoelectrochemical performance of $CuWO_4$ films

for water splitting by hydrogen treatment, Applied Surface Science, 361,133–140. http://dx.doi.org/10.1016/j.apsusc.2015.11.129

[36] N. Gaillard, Y. Chang, A.D. Angelis, S. Higgins, A. Braun (2013) A nanocomposite photoelectrode made of 2.2 eV band gap copper tungstate ($CuWO_4$) and multi-wall carbon nanotubes for solar-assisted water splitting, International Journal of Hydrogen Energy, 38, 3166. http://dx.doi.org/10.1016/j.ijhydene.2012.12.104

[37] S.M. Pourmortazavi, M. Rahimi-Nasrabadi, Y. Fazli, M. Mohammad-Zadeh (2015) Taguchi method assisted optimization of electrochemical synthesis and structural characterization of copper tungstate nanoparticles, Int. Journal of Refractory Metals and Hard Materials 51,29–34. http://dx.doi.org/10.1016/j.ijrmhm.2015.02.013

[38] C.M. Gonzalez, J.L. Dunford, X. Du, M.L. Post (2013) Characterization of carrierstatesin$CuWO_4$ thin-films at elevated temperatures, Journal of Solid-State Chemistry, 201,35–40. http://dx.doi.org/10.1016/j.jssc.2013.02.002

[39] O.Y. Khyzhun, T. Strunskus, S. Cramm, Y.M. Solonin (2005) Electronic structure of $CuWO_4$: XPS, XES and NEXAFS studies, Journal of Alloys and Compounds, 389,14–20. https://doi:10.1016/j.jallcom.2004.08.013

[40] U.M. Garcı´a-Pe´reza, A. Martı´nez-de la Cruz, J. Peral (2012) Transition metal tungstates synthesized by co-precipitation method: Basic photocatalytic properties, Electrochimica Acta, 81,227– 232. http://dx.doi.org/10.1016/j.electacta.2012.07.045

[41] T. Montini, V. Gombac, A. Hameed, L. Felisari, G. Adami, P. Forastero (2010) Synthesis, characterization and photocatalytic performance of transition metal tungstates, Chemical Physics Letters, 498,113–119. https://doi:10.1016/j.cplett.2010.08.026

[42] M. Rahmani, T. Sedaghat (2019) Nitrogen-doped $ZnWO_4$ nanophotocatalyst: synthesis, characterization and photodegradation of methylene blue under visible light, Research on Chemical Intermediates, 45,5111–5124. https://doi.org/10.1007/s11164-019-03880-7

[43] N. Alhokbany, S. M. Alshehri,J. Ahmed (2021) Synthesis, Characterization and Enhanced Visible Light Photocatalytic Performance of $ZnWO_4$-NPs@rGONanocomposites, Catalysts,11,1536. https://doi.org/10.3390/catal11121536

[44] M. Mohammadikish, M. Masteri-Farahani, and T. Mahdian (2019) Optical properties of copper tungstate nanoparticles prepared by microemulsion method, Inorganic and Nano-Metal Chemistry, 49,63–68. https://doi.org/10.1080/24701556.2019.1600550

[45] M. Ghedeir Alshammari, S. Mohammed Al-Ayed, A. Mohamed Abdelhalim, N. Laila Al-Harbi, A. Akram Qasem, A. Mohammed Yahya (2023) Fabrication of hierarchical flower-like WO_3 nanoparticles for effective metal ions sensing and catalytic degradation of organic dyes, Environmental Research, 233, 116468. https://doi.org/10.1016/j.envres.2023.116468

[46] E. Hossam Emama, B. Hanan Ahmed, Eslam Gomaa, H. Maher Helal, M. Reda Abdelhameed (2019) Doping of silver vanadate and silver tungstate nanoparticles for enhancement the photocatalytic activity of MIL-125-NH_2 in dye degradation, Journal of Photochemistry & Photobiology A: Chemistry, 383, 111986. https://doi.org/10.1016/j.jphotochem.2019.111986

[47] N. Farha, M. Saad Alshehri, M. Yuanbing, A. Tokeer (2023) Unraveling the chemoselective catalytic, photocatalytic and electrocatalytic applications of copper supported WO_3 nanosheets, Catalysis Communications, 178, 106678. https://doi.org/10.1016/j.catcom.2023.106678

[48] E.L.S. Souza, J.C. Sczancoski, I.C. Nogueira, M.A.P. Almeida, M.O. Orlandi, M.S. Li, R.A.S. Luz, M.G.R. Filho, E. Longo, L.S. Cavalcante (2017) Structural evolution, growth mechanism and photoluminescence properties of $CuWO_4$ nanocrystals, Ultrasonics Sonochemistry, 38,256–270. http://dx.doi.org/10.1016/j.ultsonch.2017.03.007

[49] R. Roshani, A. Tadjarodi (2021) Preparation of nanocomposite with different component ratios of $CuWO_4$ nanoparticles and nitrogen-doped reduced graphene oxide to compare their supercapacitive properties, Journal of Alloys and Compounds, 856,157302. https://doi.org/10.1016/j.jallcom.2020.157302

[50] B. Basu, A. Sale (1978) J. Mater. Sci. 13, 2703. ICDD card 00-033-0503

[51] S.N. Guin, D. Sanyal, K. Biswas (2016) The effect of order–disorder phase transitions and band gap evolution on the thermoelectric properties of AgCuS nanocrystals, Chemical science, 7,534–543. https://doi:10.1039/c5sc02966j

[52] L. Kihlborg, L. Gebert (1970) $CuWO_4$, a distorted wolframite-type structure,E. Acta Crystallogr., Sec. B: Struct. Crystallogr. Cryst. Chem. 26, 1020. ICDD card01-072-0616

[53] B.D. Cullity (1978) Elements of X-Ray Diffraction, Addison-Wesley.

[54] R. Roshani, A. Tadjarodi, A. Ghaffarinejad (2021) The effect of annealing temperature on the structure and supercapacitive properties of copper tungstate, Materials Letters, 293, 129644. https://doi.org/10.1016/j.matlet.2021.129644

[55] C. Kittel (2005) Introduction to solid state physics. John Wiley & Sons, Inc, United States of America.

[56] J. Ruiz-Fuertes, A. Pellicer-Porres, A. Segura, P. Rodríguez-Hernández, A. Muñoz (2014) Lattice and electronic contributions to the refractive index of $CuWO_4$, JOURNAL OF APPLIED PHYSICS, 116, 103706. https://doi:10.1063/1.4895125

[57] S. Muthamizh, R. Suresh, K. Giribabu, R. Manigandan, S. Praveen Kumar, S. Munusamy, L. Vijayalakshmi, A. Stephen, V. Narayanan (2014) Solid State Synthesis of Copper Tungstate Nanoparticles and its Electrochemical Detection of 4-chlorophenol, Solid State Physics, AIP Conf. Proc., 1591,508-510. https://doi:10.1063/1.4872655

[58] G. Suna, Q. Gao, S Tang, X. Chen, H. Liu, H Gao, X. Zhao, A Wang, X. Yu, S. Wang (2022) Facile Synthesis, Optical and Photoluminescence Properties of Copper Tungstate Phosphors with Strong Near-Infrared Photoabsorption, Russian Journal of Physical Chemistry, 96,1348–1355. https://doi:10.1134/S0036024422060097

[59] T. T. M. Hang, N. H.T. Vy, N. T. Hanh, T. D. Pham, L. T. H. Yen (2021) Facile synthesis of copper tungstate ($CuWO_4$) for novel photocatalytic degradation of tetracycline under visible light, Sustainable Chemistry and Pharmacy, 21, 100407.https://doi.org/10.1016/j.scp.2021.100407

[60] S. J. Naik, A. V. Salker (2010) Solid state studies on cobalt and copper tungstates nanomaterials, Solid State Sciences, 12,2065–2072. https://doi:10.1016/j.solidstatesciences.2010.08.028

[61] S. M. Pourmortazavi, M. R. Nasrabadi, M. K. Shalamzari, H. R. Ghaeni, S. S. Hajimirsadeghi (2013) Facile Chemical Synthesis and Characterization of Copper Tungstate Nanoparticles, Journal of Inorganic and Organometallic Polymers and Materials, 24, 333-339. https://doi:10.1007/s10904-013-9970-2

[62] B.J.Rani,G, S.Ravichandran, V.Ganesh,F.Ameen, A.Al-Sabri, R. Yuvakkumar (2018) Electrochemically active XWO_4 (X = Co, Cu, Mn, Zn) nanostructure for water splitting applications, Applied Nanoscience, 8, 1241–1258. https://doi.org/10.1007/s13204-018-0780-2

[63] X. Hu, D. Gao, Y. Li, H.Dong, W. Zhou, L. Yang, Y. Zhang(2019) Fabrication of novel $CuWO_4$ nanoparticles (NPs) for photocatalytic degradation of methylene blue in aqueous solution, SN Applied Sciences, 1, 119. https://doi.org/10.1007/s42452-018-0113-9

[64] V. Džimbeg-Malčić, Ž. Barbarić-Mikočević, K. Itrić (2011) Kubelka-Munk theory in describing optical properties of paper (I) [Kubelka-Munk teorija u opisivanjuoptičkihsvojstavapapira (I), Technical Gazette, 18,117-124. https://doi.org535.34/.36:676.017.55

[65] M.L. Myrick, M.N. Simcock, M. Baranowski, H. Brooke, S.L. Morgan, J. N. Mccutcheon (2011) The Kubelka-Munk diffuse reflectance formula revisited, Applied SpectroscopyReviews,46140–165. https://doi.org/10.1080/05704928.2010.537004

[66] M.V. Lalic, Z.S. Popovic, F.R. Vukajlovic (2011) Ab initio study of electronic, magnetic and optical properties of $CuWO_4$ tungstate, Computational Materials Science, 50,1179–1186. https://doi:10.1016/j.commatsci.2010.11.018

[67] R. Lacomba-Perales, J. Ruiz-Fuertes, D. Errandonea, D. Martınez-Garcıa, A. Segura (2008) Optical absorption of divalent metal tungstates: correlation between the band-gap energy and the cation ionic radius, EPL, 83, 37002. https://doi:10.1209/0295-5075/83/37002

[68] E. Longo, D.P. Volanti, V.M. Longo, L. Gracia, I.C. Nogueira, M.A.P. Almeida, A. N. Pinheiro, M.M. Ferrer, L.S. Cavalcante, J. Andres (2014) Toward an understanding of the growth of Ag filaments on α-Ag_2WO_4 and their photoluminescent properties: a combined experimental and theoretical study, Journal of Physical Chemistry, 118,1229–1239. https://dx.doi.org/10.1021/jp408167v

[69] R. Jolly Bose, R. Vinod Kumar, S. K. Sudheer, V. R. Reddy, V. Ganesan, V. P. Mahadevan (2012) Effect of silver incorporation in phase formation and band gap tuning of tungsten oxide thin films, American Institute of Physics,112, 114311. https://doi:10.1063/1.4768206

[70] M. J. Costa, A.E. Lima, E. P. Ribeiro, G.D. Costa, E. Longo, G. E. da Luz Jr, L. S. Cavalcante, R.D. S. Santos (2023) Transition metal tungstatesAWO_4 (A^{2+} = Fe, Co, Ni, and Cu) thin films and their photoelectrochemical behavior as photoanode for photocatalytic applications, Journal of Applied Electrochemistry,53, 1349-1367. https://doi.org/10.1007/s10800-023-01851-w

[71] Y. Tang, N. Rong, F. Liu, M. Chu, H. Dong, Y. Zhang, P. Xiao (2016) Enhancement of the photoelectrochemical performance of $CuWO_4$ films for water splitting by hydrogen treatment, Applied Surface Science, 361, 133‑140. https://doi.org/10.1016/j.apsusc.2015.11.129

[72] W. Guo, Z. Duan, O. Mabayoje, W. D. Chemelewski, P. Xiao, G. Henkelman, Y. Zhang, C. B. Mullins (2016) Improved Charge Carrier Transport of Hydrogen-Treated Coppe Tungstate: Photoelectrochemical and Computational Study, Journal of The Electrochemical Society163, H970-H975.https://doi:10.1149/2.0701610jes

[73] I.K. Konstantinou, T.A. Albani's (2004) TiO_2-assisted photocatalytic degradation of azo dyes in aqueous solution: kinetic and mechanistic investigations- A review, Applied Catalysis B: Environmental, 49,1–14.https://doi:10.1016/j.apcatb.2003.11.010

[74] U.G. Akpan, B.H. Hameed (2009) Parameters affecting the photocatalytic degradation of dyes using TiO2-based photocatalysts, Journal of Hazardous Materials, 170, 520–529. https://doi:10.1016/j.jhazmat.2009.05.039

[75] E. Forgacs, T. Cserhati, G. Oros (2004) Removal of synthetic dyes from wastewaters: a review, Environment International, 30,953– 971. https://doi:10.1016/j.envint.2004.02.001

[76] M.R. Hoffmann, S.T. Martin, W. Choi, D.W. Bahenemann (1995) Environmental application of semiconductor photocatalysis, Chemical Reviews, 95, 69–96.https://doi.org/10.1021/cr00033a004

[77] U.P. Azad, V. Ganesan, M. Pal (2011) Catalytic reduction of organic dyes at gold nanoparticles impregnated silica materials: influence of functional groups and surfactants, J. Nano Res. 13, 3951–3959,https://doi:0.1007/s11051-011-0317-z

[78] V. Vilas, D. Philip, J. Mathew (2016) Essential oil mediated synthesis of silver nanocrystals for environmental, anti-microbial and antioxidant applications, Materials Science and Engineering C, 61,429–436. http://dx.doi.org/10.1016/j.msec.2015.12.083

[79] A. Rufus, N. Sreeju, D. Philip (2019) Size tunable biosynthesis and luminescence quenching of nanostructured hematite (α-Fe_2O_3) for catalytic

degradation of organic pollutants, Journal of Physics and Chemistry of Solids, 124, 221–234. https://doi.org/10.1016/j.jpcs.2018.09.026

[80] N. Sreeju, A. Rufus, D. Philip (2017) Studies on catalytic degradation of organic pollutants and anti-bacterial property using biosynthesized CuO nanostructures, Journal of Molecular Liquids,242, 690-700.http://dx.doi.org/10.1016/j.molliq.2017.07.077

[81] R.L. Frost, L. Duong, M. Weier (2004) Raman microscopy of selected tungstate minerals, Spectrochim. Acta Part A, 60, 1853–1859. http://dx.doi.org/10.1016/j.saa.2003.10.002

IZVOD

JEDNOSTAVNA STRATEGIJA ZA SINTEZIZACIJU NANOČESTICA BAKAR-VOLFRAMATA SA POBOLJŠANOM HEMOKATALITIČKOM RAZGRADNJOM

Sve veća potražnja za efikasnim i održivim katalitičkim sistemima podstakla je nagli porast istraživanja nanočestica prelaznih metala kao katalizatora za različite hemijske reakcije. Nanočestice CuWO4 su formirane koprecipitacijom bakar-hlorida i natrijum-volframata u molarnom odnosu 1:1. Nanočestice su opširno okarakterisane korišćenjem različitih tehnika, uključujući rendgensku difrakciju (XRD), Ramanovu spektroskopiju, Furijeovu transformacionu infracrvenu (FTIR) spektroskopiju, ultraljubičasto-vidljivu difuznu refleksivnu spektroskopiju (UV-DRS), Brunauer-Emet-Telerovu (BET), rendgensku fotoelektronsku spektroskopiju (XPS), energetski disperzivnu spektroskopiju (EDS) i merenja fotoluminiscencije (PL). XRD i RAMAN studije su otkrile prisustvo molekula vode u rešetki sintetisanog i termički obrađenog uzorka na 300 °C, što ukazuje da je materijal bakar-volframat dihidrat ($CuWO_4$•$2H_2O$) sa monoklinskom strukturom. Nasuprot tome, uzorci termički obrađeni na 400 °C, 500 °C i 600 °C pokazali su anortičnu (trikliničnu) strukturu $CuWO_4$. XRD podaci su korišćeni za izračunavanje prosečne veličine zrna i parametara rešetke.FT-IR analiza potvrđuje formiranje $CuWO_4$ nanočestica. Difuznom refleksivnom ultraljubičasto-vidljivom spektroskopijom dobijene su energetske zabranjene zone nanočestica u rasponu od 2,9 do 2,2 eV, merene metodom Kubelka i Munk. Brunauer-Emet-Telerova (BET) analiza specifične površine pružila je uvid u dostupnost aktivnih površinskih mesta u $CuWO_4$ nanostrukturama. Elementarna analiza i hemijski sastav CuWO4 određeni su korišćenjem rendgenske fotoelektronske spektroskopije (XPS) i energetski disperzivne spektroskopije (EDS), što potvrđuje prisustvo vrhova koji odgovaraju samo W, O i Cu. Studija fotoluminiscencije (PL) sa talasnom dužinom pobuđivanja od 290 nm otkriva da su se za sve uzorke emisije pojavile na talasnim dužinama između 400 i 500 nm. Katalitička aktivnost CuWO4 nanočestica procenjena je merenjem razgradnje metilen plave boje. Ova studija izveštava o novoj sintezi CuWO4 kao efikasnog hemokatalizatora, postižući katalitičku razgradnju od približno 98,3%, što može imati potencijalne primene u upravljanju otpadnim vodama.

Ključne reči: *Volframat bakra, hemokataliza, metoda koprecipitacije, XRD, UV-Vis, BET, XPS*

Naučni rad
Rad primljen: 04.05.2026.
Rad prihvaćen: 06.06.2026.

Jolly Bose Raghavan Pillai https://orcid.org/0000-0002-7172-3148